# Crystallographic rotation during solid-phase epitaxy of $SrTiO_3$ from nanoscale seed crystals

Samuel D. Marks,[1] Rui Liu,[1] Yajin Chen,[1] Qian Li,[2] Steven J. Leake,[3] Donald E. Savage,[1] Susan E. Babcock,[1] Tobias U. Schülli,[3] and Paul G. Evans[1,*]

[1] *Department of Materials Science and Engineering, University of Wisconsin, Madison, WI 53706, USA*

[2] *State Key Laboratory of New Ceramics and Fine Processing, School of Materials Science and Engineering, Tsinghua University, Beijing 100084, China*

[3] *The European Synchrotron ESRF, BP 220, F-38043 Grenoble Cedex, France*

* pgevans@wisc.edu

## Abstract

The crystallization of amorphous complex oxide layers from isolated seed crystals presents the opportunity to remove geometric constraints posed by thin film epitaxial growth methods employing single-crystal substrates. The crystallization processes initiated by a distribution of isolated nanoscale seeds occur in a state of mechanical stress that is different from planar thin film epitaxy. The effects of this stress were probed in the crystallization of the model perovskite oxide $SrTiO_3$ nucleated by isolated nanoscale $SrTiO_3$ seeds. Synchrotron nanobeam scattering and diffraction was used to probe the spatial distribution of crystalline and amorphous $SrTiO_3$. Contributions to the diffraction patterns from these components were identified using non-negative matrix factorization. Individual $SrTiO_3$ crystallites exhibit a lattice rotation resulting from the density difference between amorphous and crystalline $SrTiO_3$. The crystal-amorphous interface advancing from the seeds exhibited a rotation of the crystal lattice with a rate of tens of degrees per micron of crystallization in the plane of the film. The rate of the lattice rotation provides insight

into the crystallization mechanism. The lattice rotation indicates that nanoscale morphological control during solid-phase epitaxial crystallization from nanocrystal seeds can be achieved by manipulating the interface stress between the amorphous and crystalline phases to control dislocation dynamics.

The crystallization of complex oxides from amorphous precursor layers is a promising route toward the creation of epitaxial materials and three-dimensional heterostructures with an expanded range of compositions and geometries.[1] Seeding methods based on nanocrystals or transferred membranes initiate nucleation and remove the need for a single crystal substrate.[2-4] Seeded solid-phase epitaxy (SPE) expands the possibility of developing functional epitaxial layers for geometries and materials for which templating substrates are not available, such as single crystal growth over large areas, on amorphous substrates, or on crystalline substrates with lattice symmetry that is incompatible with the crystallizing material. The crystal structure and orientation of the seed crystal provides a template for laterally crystallization.[3, 5] Complex strain states can evolve as a result of the thin film stress associated with the density changes across the crystal-amorphous interface.[6]

Nanoscale $SrTiO_3$ seed crystals were created by the crystallization of amorphous $SrTiO_3$ deposited as a very low coverage layer onto an $Si/SiO_2$ substrate. Figure 1(a) shows a schematic of the process in which the nanoscale seed crystals are formed through the crystallization of amorphous $SrTiO_3$ deposited on $SiO_2$. The low-coverage layer of $SrTiO_3$ was created by using radio-frequency magnetron sputtering to deposit $SrTiO_3$ through a shadow mask with a 100-μm diameter aperture, yielding regions of very low $SrTiO_3$ coverage beneath the edge of the shadow mask. The seeds were formed by the aggregation at 650 °C of $SrTiO_3$ into isolated crystals with a broad range of orientation and a characteristic size of 100-300 nm.[4] An SEM image showing a distribution of isolated nanoscale crystals is displayed in Fig. 1(b). Powder x-ray diffraction studies have indicated that this process results in a random crystallographic texture of the seeds.[4]

The solid-phase crystallization of initially amorphous $SrTiO_3$ at nanoscale seeds is illustrated in Fig. 2(a). The geometry in Fig. 2(a) is distinct from vapor-phase epitaxial growth of

a thin film in several ways. First, the elastic environment of three-dimensional epitaxial crystallization leads to effects that are not evident in planar epitaxy. The stress distribution is three-dimensional and occurs locally. Crystallization in a lateral direction with respect to the surface normal does not allow the stress arising from densification to be relieved uniformly. In addition, crystallization in the geometry shown in Fig. 2(a) involves the propagation of crystal-amorphous interfaces over far larger distances, on the order of micrometers rather than the tens of nanometers of typical layer thicknesses.

The complex elastic phenomena associated with solid-phase crystallization arise in part from the difference in the densities of the amorphous and crystalline forms of $SrTiO_3$. The measured density of amorphous $SrTiO_3$ is 10% less than crystalline $SrTiO_3$, with some dependence on the preparation conditions.[7] Other transition-metal complex and binary oxides, including ferroelectrics and magnetic oxides, have a similar density differences and structures and can also be crystallized via SPE.[8-11] $SrTiO_3$ is thus a model system for the broader set of problems in the crystallization of perovskite complex oxides.

The amorphous $SrTiO_3$ precursor for lateral crystallization was created by a second sputtering deposition step, which yielded a continuous amorphous layer with a thickness of 40 nm. The amorphous $SrTiO_3$ was subsequently partially crystallized by heating to 450 °C for 14 h. The crystallization of the $SrTiO_3$ overlayer begins at its interfaces with the nanocrystal seeds and occurs at an approximately constant velocity.[4] A plan view schematic and a scanning electron microscopy (SEM) image of the crystallized $SrTiO_3$ are shown in Figs. 2(b) and 2(c), respectively. The crystallization process resulted in approximately circular crystallized regions with an average diameter of 2 μm surrounded by the remaining amorphous $SrTiO_3$ layer, as shown in the SEM image of a larger region in Fig. 2(d). The region shown in Fig. 2(d) exhibits a variation in

concentration of $SrTiO_3$ crystallites that is set by the distribution of seed crystals.

The crystallized regions were characterized using grazing-incidence synchrotron x-ray nanobeam diffraction at the ID01 beamline of the European Synchrotron (ESRF).[12] An incident x-ray beam with a photon energy of 20 keV was focused to a 230 × 140 $nm^2$ full-width-at-half-maximum spot using Kirkpatrick-Baez optics. The experiments were conducted in a grazing-incidence geometry in order to maximize the volume of the amorphous material probed by the focused beam, while suppressing contributions due to thermal diffuse scattering (TDS) from the Si substrate. The grazing-incidence angle of 0.35° resulted in a beam footprint of 230 nm × 23 μm. Diffraction patterns were recorded on a pixel-array detector with a GaAs sensor with 55 μm pixels positioned 50 mm from the sample, spanning an angular range of 33°.

The x-ray nanobeam diffraction patterns show signatures of the scattering from the amorphous layer and diffraction from the crystalline seeds and the crystallized $SrTiO_3$ overlayer. Figure 3(a) shows an average of diffraction patterns collected in a 4 μm-wide linear scan using 100 nm steps. The scanned line included a region of amorphous $SrTiO_3$ that occupied the majority of the region with an isolated region of crystallized $SrTiO_3$. The amorphous and crystalline components produced distinct features in the distribution of diffracted x-ray intensity in Fig. 3(a). Figure 3(a) also exhibits several artifacts of the experimental arrangement: (i) a region spanned by the beamstop, (ii) lines of low intensity arising from the boundaries between panels of the detector, (iii) TDS from the Si substrate, and (iv) a powder diffraction ring arising from the x-ray optical elements that are easily differentiated from the scattering from the sample. The diffraction patterns were analyzed in terms of the scattering wavevector $Q=4\pi \sin(2\theta/2)/\lambda$. Here λ is the x-ray wavelength and 2θ is the scattering angle with respect to the incident beam direction. The azimuthally integrated distribution of intensity in the average diffraction pattern is shown as a

function of $Q$ in Fig. 3(b). The intensity scattered from amorphous $SrTiO_3$ appears as the diffuse ring centered at wavevector $Q$=2.09 $Å^{-1}$. The native oxide and subsequent oxidation of the Si surface during the processes associated with seed formation and the crystallization of the amorphous $SrTiO_3$ precursor result in a $SiO_2$ layer with a thickness of the order of 1 nm. No signature of the crystallization of $SiO_2$ is observed in the diffraction pattern. Scattering from amorphous $SiO_2$ has not been included in the analysis. Powder diffraction peaks corresponding to the 110, 111, and 200 reflections of $SrTiO_3$ are apparent in Fig. 3b. The reflections from {100}, {111}, and {110} families of planes appearing in Fig. 3 arise from different crystals that lie within the footprint of the x-ray beam. The orientation of the {100} family was recorded using the 200 reflections. The $SrTiO_3$ powder rings appearing Fig. 3(a) are discontinuous with a maximum of 3 distinct Bragg reflections at each probe position, indicating that 3 $SrTiO_3$ crystals met the Bragg condition in the scan. Based on the area of the beam spot and the average size of the crystals, we estimate that there are fewer than 30 crystals in the scanned area.

The contributions of the amorphous and crystallized $SrTiO_3$ to the overlapping distributions of the scattered x-ray intensity were separated by breaking the diffraction patterns into constituent components using non-negative matrix factorization (NMF). Component-based image processing has been previously employed for high-throughput data analysis of two-dimensional diffraction patterns acquired in x-ray diffraction microscopy.[13] The NMF analysis used the scikit-image software package.[14] Briefly, NMF finds non-negative matrices $X$ and $W$ such that the diffraction pattern $V$ can be expressed as $V \approx XW$. The contents of $X$ and $W$ are found without supervision by optimizing the squared Frobenius norm $d_F(V, WX) = \frac{1}{2}||V - XW||_F^2$. The vector $W$ is made up of eigenvalues by which the linear combination $\sum_i W_i X_i$ reproduces $V$.[15] The elements of $V$ correspond to the individual diffraction patterns collected during a raster scan. $X$ is a $1 \times N$ row

vector of images, where $N$ is the number of components considered in the analysis. The elements of $X$ are individual image matrices, hereafter referred to as basis diffraction patterns, containing distinct features that arise in $V$.

The eigenvalues corresponding to the first 20 components of the average detector image found by principal component analysis (PCA) are shown in Fig. 4(a). The PCA components were found without supervision. The number of components, $N$, with statistically significant eigenvalues (i.e. accounting for a meaningful amount of variance in $V$) was chosen from Fig. 4(a). The number of components required to account for the majority of the variance is apparent as an elbow in the curve.[16] Figure 4(a) exhibits a rapid decrease in eigenvalues for up to approximately four basis diffraction patterns and a far slower decrease for $N$ greater than 4.

The distributions of scattered x-ray intensity in the basis diffraction patterns resulting from the NMF analysis are shown in Fig. 4(b). The basis diffraction patterns in Fig. 4(b) are labeled $X_1$ through $X_4$ in order of the magnitude of their contribution to the average diffraction pattern, with the largest contribution coming from $X_1$. The structural origin of the intensity in the component images can be determined by analyzing the intensity distribution in each image. Basis diffraction pattern $X_1$ contains the x-ray scattering signature from the amorphous layer, TDS from the Si substrate, and diffraction from x-ray optical elements. The intensity associated with the TDS and x-ray optical elements does not vary as a function of position on the sample within the range of the scan. Basis diffraction patterns $X_2$ to $X_4$ all show diffracted intensity appearing on the each of the 110, 111, and 200 powder rings.

Figure 5 shows a series of line profiles containing the fractional contributions of each basis diffraction pattern to the diffraction patterns acquired along the scan. The four component weights at each scan point sum to 1. The weight distributions of the four basis diffraction patterns are

analogous to real space intensity distributions made by integrating diffraction signals as a function of location on a sample. The spatial profiles of the component weights in Fig. 5 indicate that the scanned region includes an area of crystallized $SrTiO_3$ surrounded by a region in which the $SrTiO_3$ has remained amorphous. The variation of the weights of the basis diffraction pattern $X_1$ along the scan show the spatial distribution of intensity originating from scattering from amorphous $SrTiO_3$. The contribution of basis diffraction patterns $X_2$ to $X_4$ are large at the scan points in which there is a local minimum in the contribution from $X_1$.

The most prominent diffraction signals within the basis diffraction patterns are three 110 reflections that appear simultaneously on the detector during the raster mapping. The angle $\chi$ describes angular position along the powder ring, as illustrated by the diagram including specific angles $\chi_a$ and $\chi_b$ on the diffraction pattern in Fig. 6(a) which correspond to the initial and final points of the azimuthal integration along $\chi$, shown in Fig. 6(b). Three reflections from {110} planes are simultaneously visible along the powder ring at distinct values of $\chi$ in basis diffraction patterns $X_2$, $X_3$, and $X_4$. The asterisk in Fig. 6(a) indicates an artifact arising from an x-ray optical element. The reflections from {110} planes are separated by $\Delta\chi = 60°$, measured using distribution of the intensity in Fig. 6(b). The three diffracted intensity maxima in Fig. 6(b) arise from diffraction from the {110} planes within the same crystals. Multiple reflections appear for each crystal because the high mosaicity makes it possible for reflections with Bragg angles separated by a few degrees to meet the Bragg condition. The cubic structure of $SrTiO_3$ causes reflections in the {110} family to be separated by 60° along $\chi$ when the incident beam is approximately along the [111] direction.

Line scans across several $SrTiO_3$ crystallites reveal that there is a position-dependent shift of the intensity in the 110, 111 and 200 powder rings along the $\chi$ direction on the detector. The angular shift corresponds to the rotation of the scattering wavevector about the zone axis. Figure 7(a) shows

a single diffraction pattern in which three 110 variants are visible, along with an artifact indicated by an asterisk. Three regions of interest (ROIs) labeled $\chi_1$, $\chi_2$, and $\chi_3$ are drawn in one of the variants centered at different values of $\chi$ along the 110 powder ring. Each ROI spans an angular range of 4.3° along $\chi$. The spatial map of the integrated intensity from within each ROI is plotted in Fig. 7(b). The crystalline region being probed is composed of separate domains in which the crystal surface normal of each neighboring domain is tilted, resulting in a rotation of the scattering plane that produces a relative angular shift of the 110 reflections along the $\chi$ direction. The reflections shown in Figs. 3 and 7 exhibit the same rotation as a function of position. The rotation is consistent with an interpretation in which those reflections arise from a single crystal with a shared zone axis.

The redistribution of the intensity along $\chi$ corresponds to a continuous reorientation of the unit cell with distance from the seed in the laterally crystallized $SrTiO_3$ region. The magnitude of the lattice rotation at each sample position was determined by measuring the rotation in $\chi$ of the intensity in the 110, 111 and 200 reflections. Sections of the powder rings containing each reflection were divided into ROIs separated along $\chi$ by 2.25°. Matrix factorization of these ROIs using two components was performed, with the amorphous scattering and crystalline diffraction signals separated into the first and second components, respectively. The component weights were found as a function of beam position in the line scan.

The angular shift is plotted as a function of the position of the centroid of the intensity of the crystalline component in Fig. 7(c). The angle at the center of the crystalline region is $\chi_{cen}$. Two scans of offset regions of the crystallite producing reflections from {110} families of planes are labelled as {110} crystal, region 1 and {110} crystal, region 2 in Fig. 7(c). The mean rate of rotation of the three crystals shown in Fig. 7(c) is 25° per μm with a standard deviation of 4° per μm. The similarity of the rotation rates among these crystals indicates that similar defect formation

processes are occurring in each crystal.

The crystalline region of the sample producing the diffracted intensity along the 110 variants spans a distance of 2 μm. The intensity within each 110 variant rotates along the χ direction by 46° as the beam is scanned across the crystalline $SrTiO_3$ region. The continuous rotations of the diffracted intensity of the 110 reflection variants along the χ direction as a function of location result from the rotation of the crystal. Figure 7(d) illustrates a cross-sectional view of the laterally crystallized $SrTiO_3$ with rotating crystallographic planes indicated by the black arrows. In this microstructural model, the incremental lattice rotation axis is in the plane of the film surface and orthogonal to the direction of the crystallization. The fixed incident angle of the x-ray probe leads to an experimental arrangement in which the Bragg condition can only be satisfied by crystals that rotate around a rotation axis approximately parallel to the incident x-ray wavevector. In the radially crystallized regions of $SrTiO_3$, this corresponds to a thin slice of the crystallized region extending along the scan direction. This assumption is tested in a calculation of the scattering geometry that would result from this experimental arrangement, described in Supporting Information. The small variation of the Bragg condition due to the requirement to couple the crystal rotation and in-plane orientation results in a width of on the order of 50 nm for this region (see Fig. S3(b)). Other directions of the lattice rotation cause the crystal to tilt out of the Bragg condition.

The lattice rotation apparent in Fig. 7(c) is consistent with the large tensile stresses at crystal-amorphous interfaces due to the change in density across the interface. Tensile stress in the crystalline material at crystal-amorphous interfaces have been previously reported in systems that undergo significant densification during crystallization such as $SiO_2$, $GeO_2$, and $Sb_2S_3$.[17, 18] The stress is a key feature of the mechanism driving the rotation of the crystal lattice during crystallization. Tensile stress exerted on the crystal by the less dense amorphous material induces

a strain state that provides the elastic energy needed to form dislocations. The dislocation density, ρ, required to produce the measured lattice rotation can be approximated by

$$\rho = \frac{(\chi_{cen} - \chi)_{tot}}{|\mathbf{b}|d},$$

where $(\chi_{cen} - \chi)_{tot}$ is the total rotation of the 110 reflections, |**b**| is the Burger's vector, and $d$ is the length of the crystalline $SrTiO_3$ region.[19] We adopt the value of **b** for $SrTiO_3$ unit cell equal to the lattice constant 3.905 Å, as determined for the relaxation of epitaxial $SrTiO_3$.[20] Assuming a homogeneous distribution, the dislocation density needed to produce the observed rotation is found to be $1 \times 10^{15}$ $m^{-2}$. The estimated magnitude of the dislocation density in $SrTiO_3$ formed through lateral SPE is slightly higher than reported for bulk $SrTiO_3$ that has undergone high temperature deformation.[21] However, dislocation densities of similar magnitude have been reported in mechanically polished bulk $SrTiO_3$ within a 5 μm region beneath the surface.[22, 23]

Further insight into the possible role of plastic deformation can be obtained by comparing the scale of possible elastic stress in the problem with the threshold stress for plastic deformation in $SrTiO_3$. The reported room-temperature yield strength of $SrTiO_3$ is 120 MPa.[24] Elastic deformation leading to the observed lattice rotation would lead to a curvature-induced stress on the order of 1 GPa. Similarly, purely elastic accommodation of the density difference between amorphous and crystalline $SrTiO_3$ would also lead to stress on the order of 1 GPa. In both cases the elastic stress greatly exceeds the reported yield strength, making plastic deformation likely.

**Conclusion**

High energy synchrotron x-ray nanobeam microscopy shows that extreme lattice rotation arises in the solid-phase crystallization of amorphous $SrTiO_3$ from isolated seed crystals. A machine learning approach distinguishes overlapping contributions to the diffraction patterns from

amorphous scattering and crystalline diffraction using non-negative matrix factorization. A lattice rotation of 46° in a distance of 2 μm across laterally crystallized $SrTiO_3$ is observed within an isolated crystalline region surrounded by an amorphous $SrTiO_3$ matrix. The rotation rate is constant among multiple crystals, indicating that kinetic and elastic processes occurring during crystallization set the rotation rate. The continuous crystallographic reorientation as a function of distance from the seed crystal is consistent with the propagation of dislocations that nucleate in response to the tensile stress exerted on the crystal from the amorphous layer. Remarkably, the reorientation is locally continuous, rather than resulting in a series of discrete polycrystalline grains. Further progress in understanding the mechanical processes through which the microstructure evolves during crystallization can potentially lead to processing conditions that favor or inhibit dislocation motion and can, in principle, lead to new ways to control the crystal orientation and microstructure.

**Acknowledgements**

This research was primarily supported by NSF through the University of Wisconsin Materials Research Science and Engineering Center (DMR-1720415).

**Conflict of Interest**

The authors declare no conflict of interest.

**Supporting Information**

Calculations of the scattering geometry for scanning x-ray diffraction microscopy in circular rotating lattice crystals are provided in Supporting Information. These calculations include analysis of paths through rotating lattice crystals along which the Bragg condition is met during fixed-incident-angle microscopy experiments.

**References**


1. Guo, L.; Campbell, N.; Choi, Y.; Kim, J.-W.; Ryan, P. J.; Huyan, H.; Li, L.; Nan, T.; Kang, J.-H.; Sundahl, C., Spontaneous Hall effect enhanced by local Ir moments in epitaxial $Pr_2Ir_2O_7$ thin films. *Phys. Rev. B* **2020,** *101* (10), 104405.

2. Boileau, A.; Hurand, S.; Baudouin, F.; Lüders, U.; Dallocchio, M.; Bérini, B.; Cheikh, A.; David, A.; Paumier, F.; Girardeau, T., Highly Transparent and Conductive Indium-Free Vanadates Crystallized at Reduced Temperature on Glass Using a 2D Transparent Nanosheet Seed Layer. *Adv. Funct. Mater.* **2021**, 2108047.

3. Taira, K.; Hirose, Y.; Nakao, S.; Yamada, N.; Kogure, T.; Shibata, T.; Sasaki, T.; Hasegawa, T., Lateral Solid-Phase Epitaxy of Oxide Thin Films on Glass Substrate Seeded with Oxide Nanosheets. *ACS Nano* **2014,** *8* (6), 6145-6150.

4. Chen, Y.; Tilka, J. A.; Ahn, Y.; Park, J.; Pateras, A.; Zhou, T.; Savage, D. E.; McNulty, I.; Holt, M. V.; Paskiewicz, D. M., Seeded Lateral Solid-Phase Crystallization of the Perovskite Oxide $SrTiO_3$. *J. Phys. Chem. C* **2019,** *123* (12), 7447-7456.

5. Maret, H.; Weisberg, D.; Chan, H. M.; Strandwitz, N. C., Seeded solid-phase epitaxy of atomic layer deposited aluminum oxide. *Cryst. Growth Des.* **2016,** *16* (3), 1662-1666.

6. Evans, P.; Savage, D.; Prance, J.; Simmons, C.; Lagally, M.; Coppersmith, S.; Eriksson, M.; Schülli, T., Nanoscale Distortions of Si Quantum Wells in Si/SiGe Quantum-Electronic Heterostructures. *Adv. Mater.* **2012,** *24* (38), 5217-5221.

7. Chen, Y.; Yusuf, M. H.; Guan, Y.; Jacobson, R.; Lagally, M. G.; Babcock, S. E.; Kuech, T. F.; Evans, P. G., Distinct Nucleation and Growth Kinetics of Amorphous $SrTiO_3$ on (001) $SrTiO_3$ and $SiO_2$/Si: A Step toward New Architectures. *ACS Appl. Mater. Interfaces* **2017,** *9* (46),

41034-41042.

8. Krockenberger, Y.; Matsui, H.; Hasegawa, T.; Kawasaki, M.; Tokura, Y., Solid phase epitaxy of ferrimagnetic $Y_3Fe_5O_{12}$ garnet thin films. *Appl. Phys. Lett.* **2008,** *93* (9), 092505.

9. Marks, S. D.; Lin, L.; Zuo, P.; Strohbeen, P. J.; Jacobs, R.; Du, D.; Waldvogel, J. R.; Liu, R.; Savage, D. E.; Booske, J. H.; Kawasaki, J. K.; Babcock, S. E.; Morgan, D.; Evans, P. G., Solid-phase epitaxial growth of the correlated-electron transparent conducting oxide $SrVO_3$. *Phys. Rev. Mater.* **2021,** *5* (8), 083402.

10. Waduge, W. L.; Chen, Y.; Zuo, P.; Jayakodiarachchi, N.; Kuech, T. F.; Babcock, S. E.; Evans, P. G.; Winter, C. H., Solid-Phase Epitaxy of Perovskite High Dielectric $PrAlO_3$ Films Grown by Atomic Layer Deposition for Use in Two-Dimensional Electronics and Memory Devices. *ACS Appl. Nano Mater.* **2019,** *2* (11), 7449-7458.

11. Nashimoto, K.; Fork, D.; Anderson, G., Solid phase epitaxial growth of sol-gel derived Pb(Zr, Ti)$O_3$ thin films on $SrTiO_3$ and MgO. *Appl. Phys. Lett.* **1995,** *66* (7), 822-824.

12. Leake, S. J.; Chahine, G. A.; Djazouli, H.; Zhou, T.; Richter, C.; Hilhorst, J.; Petit, L.; Richard, M.-I.; Morawe, C.; Barrett, R., The Nanodiffraction beamline ID01/ESRF: a microscope for imaging strain and structure. *J. Synchrotron Radiat.* **2019,** *26* (2), 571-584.

13. Laanait, N.; Zhang, Z.; Schlepütz, C. M., Imaging nanoscale lattice variations by machine learning of x-ray diffraction microscopy data. *Nanotechnology* **2016,** *27* (37), 374002.

14. Van der Walt, S.; Schönberger, J. L.; Nunez-Iglesias, J.; Boulogne, F.; Warner, J. D.; Yager, N.; Gouillart, E.; Yu, T., scikit-image: image processing in Python. *PeerJ* **2014,** *2*, e453.

15. Lee, D. D.; Seung, H. S., Learning the parts of objects by non-negative matrix factorization. *Nature* **1999,** *401* (6755), 788-791.

16. Cattell, R. B., The scree test for the number of factors. *Multivar. Behav. Res.* **1966,** *1* (2), 245-276.

17. Musterman, E. J.; Savytskii, D.; Dierolf, V.; Jain, H., The source of lattice rotation in rotating lattice single (RLS) crystals. *Scripta Mater.* **2021,** *193*, 22-26.

18. Savytskii, D.; Jain, H.; Tamura, N.; Dierolf, V., Rotating lattice single crystal architecture on the surface of glass. *Sci. Rep.* **2016,** *6* (1), 1-10.

19. Lutjes, N. R.; Zhou, S.; Antoja-Lleonart, J.; Noheda, B.; Ocelík, V., Spherulitic and rotational crystal growth of Quartz thin films. *Sci. Rep.* **2021,** *11* (1), 14888.

20. Qin, Y.; Jia, C.; Urban, K.; Hao, J.; Xi, X., Dislocations in SrTiO3 thin films grown on LaAlO3 substrates. *J. Mater. Res.* **2002,** *17* (12), 3117-3126.

21. Johanning, M.; Porz, L.; Dong, J.; Nakamura, A.; Li, J.-F.; Rödel, J., Influence of dislocations on thermal conductivity of strontium titanate. *Appl. Phys. Lett.* **2020,** *117* (2), 021902.

22. Porz, L.; Frömling, T.; Nakamura, A.; Li, N.; Maruyama, R.; Matsunaga, K.; Gao, P.; Simons, H.; Dietz, C.; Rohnke, M.; Janek, J.; Rödel, J., Conceptual Framework for Dislocation-Modified Conductivity in Oxide Ceramics Deconvoluting Mesoscopic Structure, Core, and Space Charge Exemplified for $SrTiO_3$. *ACS Nano* **2021,** *15* (6), 9355-9367.

23. Jin, L.; Guo, X.; Jia, C., TEM study of< 110>-type 35.26° dislocations specially induced by polishing of SrTiO3 single crystals. *Ultramicroscopy* **2013,** *134*, 77-85.

24. Patterson, E. A.; Major, M.; Donner, W.; Durst, K.; Webber, K. G.; Rödel, J., Temperature-Dependent Deformation and Dislocation Density in $SrTiO_3$ (001) Single Crystals. *J. Am. Ceram. Soc.* **2016,** *99* (10), 3411-3420.

**Figure 1**: (a) Formation of $SrTiO_3$ seed crystals through crystallization of a low-coverage amorphous $SrTiO_3$ deposited through a shadow mask. (b) SEM micrograph showing the resulting distribution of crystallized $SrTiO_3$ seeds near the edge of the masked regions.

**Figure 2**: (a) Cross-sectional schematic of amorphous $SrTiO_3$ on the nanocrystal seeds. Subsequent heating results in the propagation of the amorphous overlayer/nanocrystal interface away from the seed. (b) Plan-view schematic of a circular region of laterally crystallized $SrTiO_3$ (red) around a nanocrystal seed (black box). (c) SEM image showing $SrTiO_3$ grown laterally via solid-phase epitaxy from nanocrystal seed. (d) SEM micrograph of an area with a gradient in the concentration of crystalline seeds and a corresponding variation in in the concentration of laterally crystallized $SrTiO_3$.

**Figure 3**: (a) Average x-ray area detector image from a scanning x-ray nanobeam diffraction scan. The white circle and black dot are shadow of the center stop and the position of the transmitted x-ray beam, respectively. (b) Azimuthally integrated diffraction and scattering profile of the average detector image in (a). The $SrTiO_3$ reflections are labeled with their indices. The symbols a, *, and ** denote scattering from amorphous $SrTiO_3$, an artifact arising from diffraction from a Pt aperture in the incident beam optics, and edge effects from the detector chip border leading to higher pixel intensities, respectively.

**Figure 4**: (a) Component eigenvalue as a function of component number derived from the principal component analysis of the average detector image from the raster scan. (b) Basis diffraction patterns containing scattering signals from the amorphous layer and detector artifacts ($X_1$) and diffraction signals from the crystalline $SrTiO_3$ regions ($X_2$, $X3$, and $X_4$). The intensity scale for each basis diffraction pattern is normalized to 1 at its maximum.

**Figure 5**: Component weight as a function of position. $W_1$ corresponds to the spatial distribution of scattered intensity from amorphous $SrTiO_3$. $W_2$, $W_3$, and $W_4$ represent the spatial distribution of diffracted intensity from crystalline $SrTiO_3$.

**Figure 6:** (a) Diffraction pattern acquired from the region of crystalline $SrTiO_3$ with vectors pointing to two points along the 110 ring, $\chi_a$ and $\chi_b$, along with their angular separation, $\Delta\chi$. An artifact from an x-ray optical element is indicated with an asterisk. (b) Line profile showing the distribution of intensity along the $\chi$ direction in an angular range encompassing the three 110 variants visible in the diffraction pattern in (a).

**Figure 7**: (a) Diffraction pattern acquired from a region of crystalline $SrTiO_3$ showing three 110 variants. The rectangles indicate ROIs centered at different $\chi$ angles for a single 110 variant. (b) Integrated intensity within the ROIs defined in (a) as a function of position. The shift of the diffracted intensity along $\chi$ as a function of position leads to maxima at different positions in each curve. (c) Lattice rotation as a function of position for crystals producing reflections from {110}, {111} and {100} families of planes from crystals in the area probed in the x-ray experiment. The {100} planes were probed using a 200 reflection. The two curves labeled {110} crystal, region 1 and {110} crystal, region 2 arise from scans of different range within the crystal producing the 110 Bragg reflections. (d) Schematic indicating rotation of the crystallographic orientation as a function of position within the crystalline $SrTiO_3$ region.

**Marks *et al.* Figure 1**

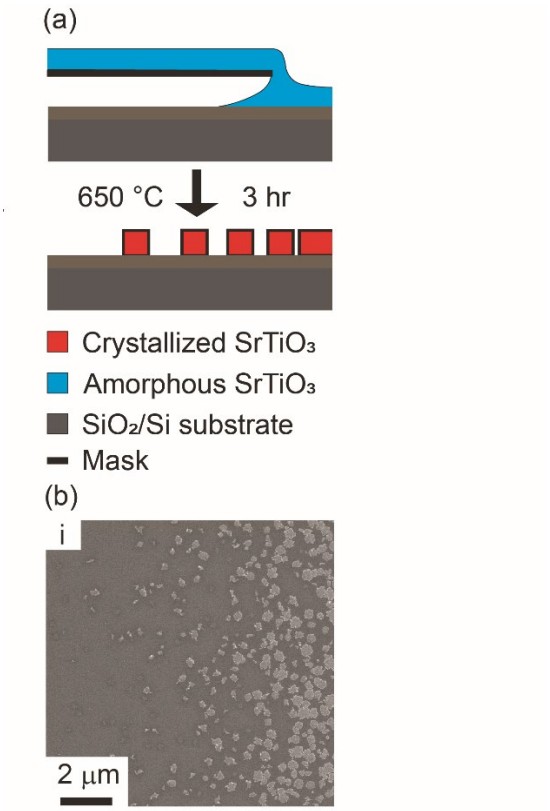

**Marks *et al.* Figure 2**

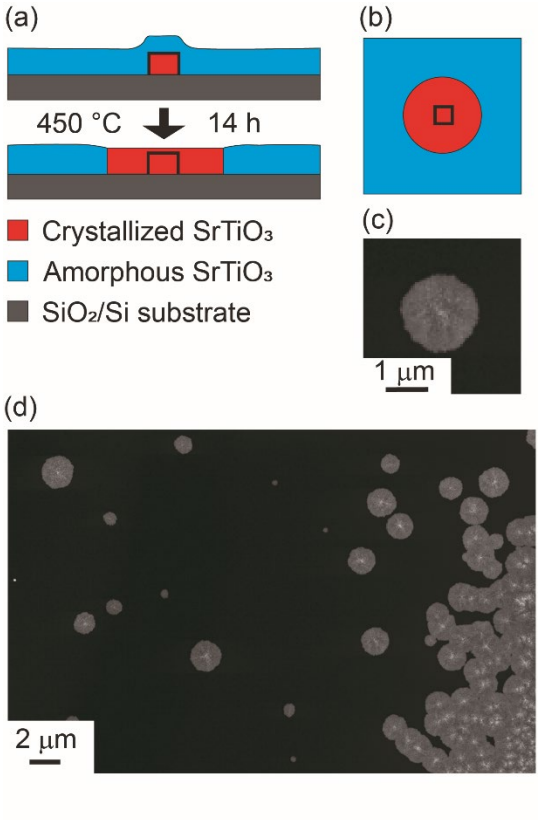

**Marks *et al.* Figure 3**

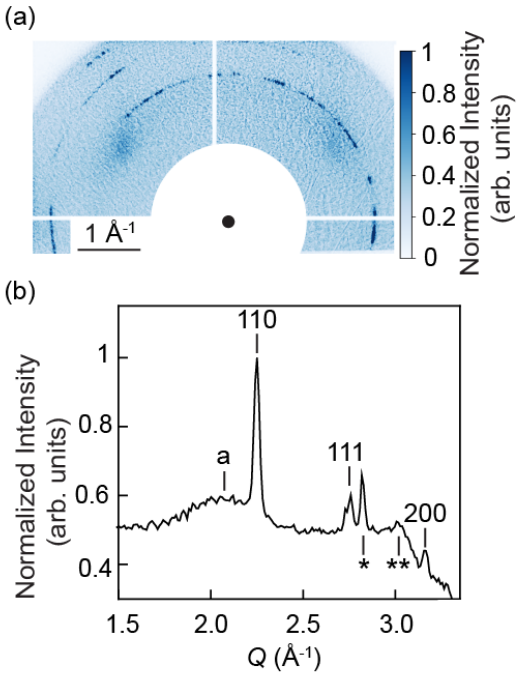

**Marks *et al.* Figure 4**

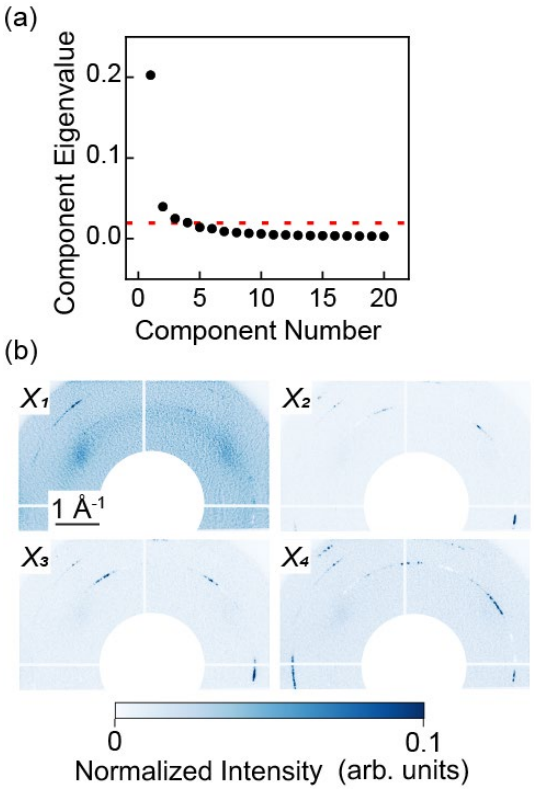

**Marks *et al.* Figure 5**

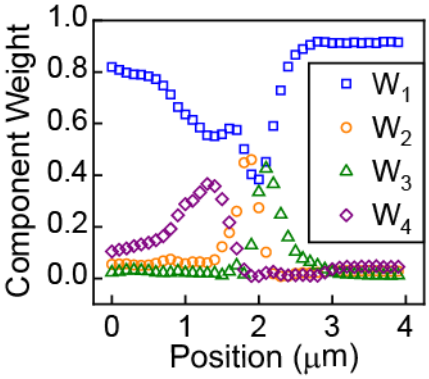

**Marks *et al*., Figure 6**

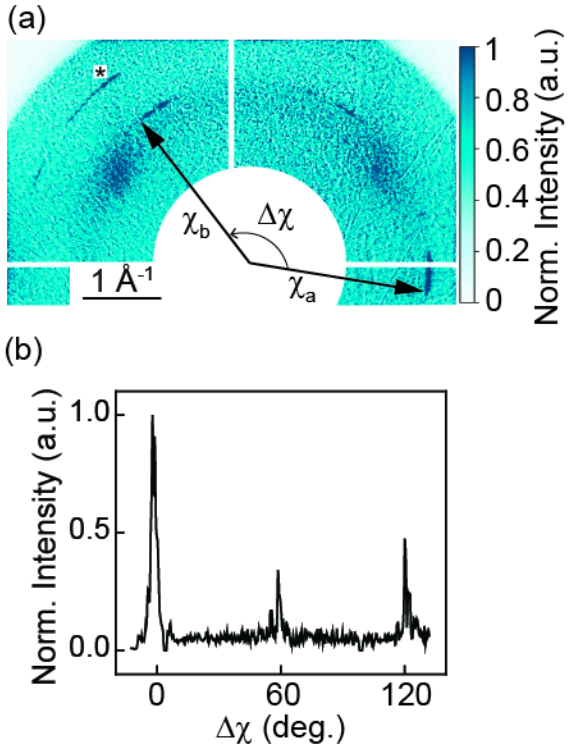

**Marks *et al*. Figure 7**

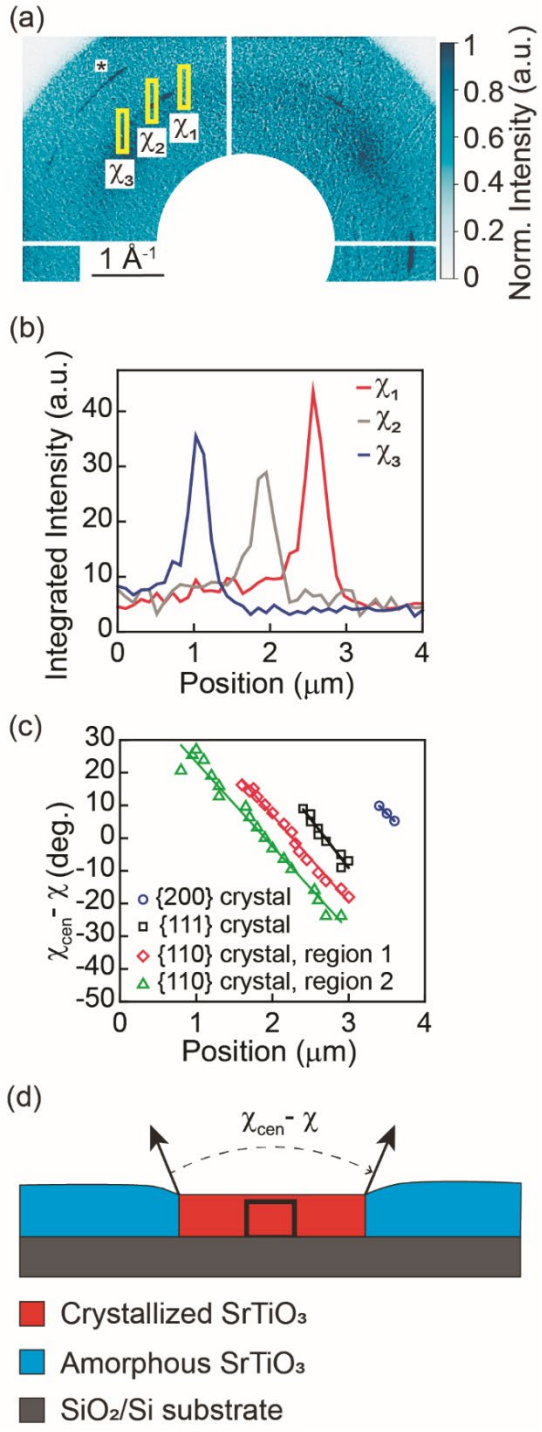

**For Table of Contents Use Only:**

**Crystallographic rotation during solid-phase epitaxy of $SrTiO_3$ from nanoscale seed crystals**

Samuel D. Marks,[1] Rui Liu,[1] Yajin Chen,[1] Qian Li,[2] Steven J. Leake,[3] Donald E. Savage,[1] Susan E. Babcock,[1] Tobias U. Schülli,[3] and Paul G. Evans[1,*]

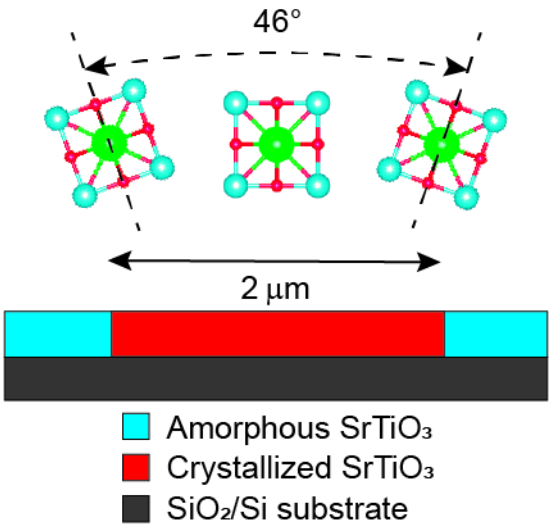


**Synopsis**

Crystallization of amorphous complex oxides by solid-phase epitaxy along in-plane directions from nanoscale seed crystals results in continuous lattice rotation. High-energy synchrotron x-ray diffraction microscopy reveals a rotation in the out-of-plane lattice vector the varies as a function of lateral crystallization distance. The density difference across the crystal-amorphous interface induces a mechanical stress state in the crystal that produces a lattice rotation of nearly 25 °/µm.